ANNUAL REVIEWS

Annual Review of Condensed Matter Physics

Liquid Crystal Colloids

Ivan I. Smalyukh[1,2]

[1]Department of Physics and Department of Electrical, Computer, and Energy Engineering, Soft Materials Research Center and Materials Science and Engineering Program, University of Colorado, Boulder, Colorado 80309, USA; email: ivan.smalyukh@colorado.edu

[2]Renewable and Sustainable Energy Institute, National Renewable Energy Laboratory and University of Colorado, Boulder, Colorado 80309, USA

Annu. Rev. Condens. Matter Phys. 2018. 9:207–26

First published as a Review in Advance on December 8, 2017

The *Annual Review of Condensed Matter Physics* is online at conmatphys.annualreviews.org

https://doi.org/10.1146/annurev-conmatphys-033117-054102

Keywords

nematic, topology, self-assembly, colloidal crystal, elasticity, multipole expansion

Abstract

Colloids are abundant in nature, science, and technology, with examples ranging from milk to quantum dots and the colloidal atom paradigm. Similarly, liquid crystal ordering is important in contexts ranging from biological membranes to laboratory models of cosmic strings and liquid crystal displays in consumer devices. Some of the most exciting recent developments in both of these soft matter fields emerge at their interface, in the fast-growing research arena of liquid crystal colloids. Mesoscale self-assembly in such systems may lead to artificial materials and to structures with emergent physical behavior arising from patterning of molecular order and nano- or microparticles into precisely controlled configurations. Liquid crystal colloids show exceptional promise for new discovery that may impinge on composite material fabrication, low-dimensional topology, photonics, and so on. Starting from physical underpinnings, I review the state of the art in this fast-growing field, with a focus on its scientific and technological potential.

1. INTRODUCTION

Colloids: microscopically dispersed gas, solid, or liquid nanometer- or micrometer-sized particles of one substance that are kept suspended throughout another substance by thermal fluctuations

Liquid crystals (LCs): soft matter systems that stand between crystalline solids and isotropic fluids and combine the properties of fluidity with orientational ordering

Colloids are soft matter systems in which microscopic particles of one substance are suspended throughout another substance (1). These gas, solid, or liquid particles, each with typical dimensions ranging from nanometers to micrometers, are kept suspended in the host surrounding medium by thermal fluctuations (1). Widely familiar naturally occurring colloids include fog, paint, and milk, whereas colloidal dispersions of synthetic particles, such as quantum dots and plasmonic nanoparticles, promise to revolutionize modern technologies and consumer products ranging from new generations of solar cells to information displays (1–3). Colloids can form liquid, crystalline, and glassy condensed matter states (1), which often serve as model systems for understanding the physics of their molecular and atomic counterparts. Colloids also offer the possibility of harnessing self-assembly to realize unusual composite materials and to understand the complex behavior of biological systems (1–3).

Liquid crystals (LCs), another important class of soft matter systems, are formed by weakly interacting anisotropic building blocks, such as molecules or micelles with anisometric rodlike or disclike shapes (1). These molecules self-organize in states with orientational order that are liquids (they flow) but exhibit elastic-type stiffness to certain orientational deformations such that they also display anisotropic properties and elastic behavior typically associated with solids (1). Weak external stimuli can dramatically alter interactions between the building blocks of LCs, so that, for example, LCs can melt into isotropic fluids as a result of modest temperature changes or can respond to low-voltage electric fields (1). This facile response to weak electric fields and other external stimuli enables many practical applications of LCs, ranging from information displays to biomedical detectors.

LC colloids are formed by dispersions of colloidal particles in the LC host medium rather than in conventional isotropic liquids (2). The discovery of novel colloidal interactions in LCs (2), which are mediated by the elasticity of the LC medium hosting the colloidal nanometer- or micrometer-sized particles, prompted the emergence of a new subfield of soft matter at the interface of LC and colloidal sciences. The fast growth of this new research arena is fueled by the richness of fundamental physics phenomena and a strong potential for technological applications. LC colloids further bridge colloidal and LC sciences within fields as diverse as topology, biology, and photonics (2–7). They may enable technological breakthroughs in the development of flexible information displays; the efficient conversion of solar energy to electricity; and the tunable photonic crystals and metamaterials and other novel optically controlled materials capable, in turn, of controlling light. For example, LC colloids may allow for realizing artificial composite materials with pre-engineered optical and mechanical properties defined through exquisite control of the structural organization of metal and semiconductor nanoparticles at mesoscopic scales, as I discuss in Section 8. The excitement that LC colloids bring from the fundamental science standpoint stems from their hierarchy of important length scales and timescales, which leads to the creation of entirely new concepts and generalizations. Two decades after its origin (2, 8–15), the field of LC colloids has become a well-established, fast-growing area of soft matter research. The main goal of this review is to summarize the recent key developments in this field and to provide an overview of the dazzling variety of current activities and future developments emerging on the horizon, with a focus on colloidal dispersions with LC building blocks much smaller than colloidal particles (**Figure 1*a***).

2. LIQUID CRYSTAL–COLLOIDAL INTERFACES, BOUNDARY CONDITIONS, AND ORIENTATIONAL ELASTICITY

One key difference between conventional isotropic host–based and LC colloids is that the molecular interactions at the interfaces of colloidal particles and the surrounding LC are highly anisotropic

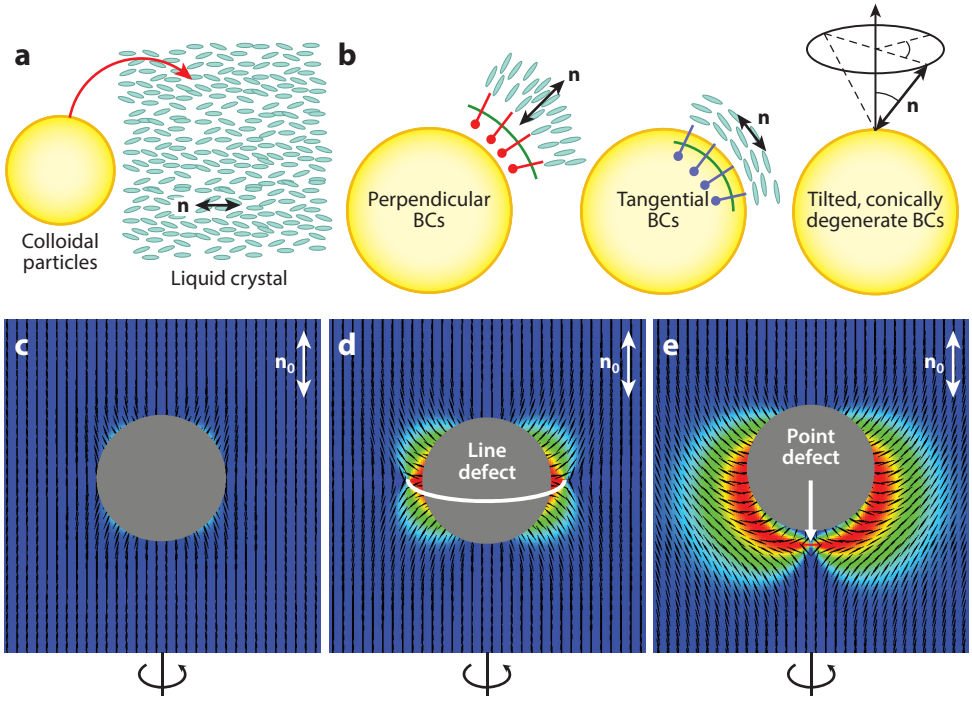

Figure 1

Liquid crystal (LC) colloids and control of surface boundary conditions (BCs). (*a*) Schematic showing colloidal particles with dimensions roughly in the range 10 nm–10 μm dispersed in LC composed of rodlike molecules approximately 1 nm in length. The director **n** represents the average direction of ordering of anisotropic building blocks such as molecules in LC phases. (*b*) Surface functionalization or natural material behavior of particles enables the control of surface BCs for **n** to be perpendicular (*left*), tangential (*middle*), or tilted and conically degenerate (*right*). (*c–e*) Interplay of elastic and surface anchoring forces defines configurations of the director field $\mathbf{n}(\mathbf{r})$, ranging from (*c*) director structure with weak deviations of $\mathbf{n}(\mathbf{r})$ away from $\mathbf{n}_0$ (the far-field uniform director) and violation of BCs at the particle surface for $D \ll \xi_e$ to the structures with (*d*) ringlike line and (*e*) pointlike topological defects that are observed at $D > \xi_e$. D is the diameter of the colloidal particle; $\xi_e = K/W$ is the extrapolation length, where $K = (K_{11} + K_{22} + K_{33})/3$ is the average elastic constant [K_{11}, K_{22}, and K_{33} are Frank elastic constants that pertain to splay, twist, and bend distortions of $\mathbf{n}(\mathbf{r})$, respectively]. The colors highlight deviations of $\mathbf{n}(\mathbf{r})$ away from $\mathbf{n}_0$, depicting regions with $\mathbf{n}(\mathbf{r})$ along $\mathbf{n}_0$ (*blue*) and regions with $\mathbf{n}(\mathbf{r})$ tilted away from $\mathbf{n}_0$ to progressively larger angles (from smallest to largest: *cyan*, *green*, *yellow*, and *red*).

(**Figure 1**). These interactions are characterized by the easy-axis orientation of the LC director **n** (the average direction of ordering of anisotropic building blocks such as molecules in LC phases) at the particle's surface with respect to the local surface normal, which depends on the particle's chemical composition and surface morphology and is controlled by chemical functionalization and other means. Similar to the case of flat surfaces (1, 15–17), boundary conditions (BCs) on colloidal particles can define the energy-minimizing local orientation of **n** to be tangential, perpendicular, or tilted with respect to the surfaces (**Figure 1*b***). In a uniformly aligned nematic phase LC, the director field $\mathbf{n}(\mathbf{r})$ is subjected to both the BCs on particle surfaces and the far-field uniform alignment of the director, $\mathbf{n}_0$. BCs are characterized by the surface anchoring energy and a corresponding coefficient W. Typically, $W < 1$ mJ/m^2, which is much smaller than the isotropic

LC director (n): average direction of ordering of anisotropic building blocks of LC phases with nonpolar $\mathbf{n} \equiv -\mathbf{n}$ symmetry

part of the corresponding surface energy. For example, in the case of perpendicular BCs with the easy axis **v** (a unit vector) locally orthogonal to the particle surface, the surface anchoring free energy can be expressed as an integral over the particle surface (18):

$$F_{\text{anchoring}} = -\frac{W}{2}\int (\mathbf{v}\cdot\mathbf{n})^2 \mathrm{d}S. \qquad 1.$$

The bulk free energy due to orientational elasticity of a nematic LC reads as (1, 18)

$$F_{\text{elastic}} = \int \left\{ \frac{K_{11}}{2}(\nabla\cdot\mathbf{n})^2 + \frac{K_{22}}{2}[\mathbf{n}\cdot(\nabla\times\mathbf{n})]^2 + \frac{K_{33}}{2}[\mathbf{n}\times(\nabla\times\mathbf{n})]^2 \right\} \mathrm{d}V, \qquad 2.$$

where K_{11}, K_{22}, and K_{33} are Frank elastic constants that pertain to splay, twist, and bend distortions of $\mathbf{n}(\mathbf{r})$, respectively, and the integration is done over the sample's volume. The LC–particle interactions are determined by a competition of bulk elastic and surface anchoring energies, which is characterized by the so-called extrapolation length $\xi_e = K/W$, where $K = (K_{11} + K_{22} + K_{33})/3$ is the average elastic constant (typically within 1–20 pN, say $K \approx 6.5$ pN for pentylcyanobiphenyl) and W is typically within 10^{-4}–10^{-6} J/m^2. When the colloidal particle's diameter $D \ll \xi_e$ (ξ_e is within 50–10,000 nm), it induces no defects and distortions of $\mathbf{n}(\mathbf{r})$ can be neglected (**Figure 1*c***). The director in this case stays aligned along $\mathbf{n}_0$ while violating BCs on the colloidal surface. In contrast, elastic distortions and bulk or surface topological LC defects (singularities) occur when $D \gg \xi_e$, in which case the BCs are met and matched to $\mathbf{n}_0$ by distorting $\mathbf{n}(\mathbf{r})$ around the particle. The emergence of line and point defects in the latter case (1, 12, 18) is illustrated by the example of perpendicular BCs in **Figure 1*d*,*e***. Overall, the structural configurations of $\mathbf{n}(\mathbf{r})$ are determined by minimization of the total free energy, the sum of Equations 1 and 2. Because the bulk elastic free energy roughly scales as $\propto KD$ and the surface energy as $\propto WD^2$, the total free energy minimization leads to violations of BCs for small D and W and to elastic distortions and defects in the opposite case. Similar considerations also apply to the cases of tangential and tilted BCs. The nature of particle-induced defects depends on the particle's topology and geometry, as discussed in Section 7.

Nematic phase: LC phase formed by anisotropic (e.g., rodlike or disclike) molecules, particles, or micelles exhibiting long-range orientational order but no positional order

Surface anchoring: anisotropic part of the surface energy describing the dependence of surface energy on orientation of **n** at LC surfaces

LC defect (singularity): a discontinuity in **n** that cannot be removed via smooth deformations

3. ELASTIC MULTIPOLES

Multipole expansion, which physicists and engineers learn as part of an undergraduate-level introduction to electromagnetism (19), is widely used in many branches of physics and cosmology. In describing the far-field distortions in electric, magnetic, gravitational, and other fields, say due to localized charge or current distributions, truncation of the multipole expansion to its leading-order nonzero term is useful for theoretical calculations and for explaining physical behavior (19). The leading-order multipoles are typically monopoles, dipoles, and quadrupoles, with higher-order multipoles rarely playing dominant roles, though they can be important for certain types of nematic colloids (see below) (2, 8–13, 20–24). Much like in the case of electrostatic charge distributions, the far-field distortions of $\mathbf{n}(\mathbf{r})$ due to a colloidal particle can be represented as elastic multipoles (2, 13, 20–24). Far from a colloidal particle, the deviations of the director n_μ ($\mu = x; y$) from the far-field uniform director $\mathbf{n}_0 = (0, 0, 1)$ are small (24, 25). Assuming one-elastic-constant approximation and representing the field as $\mathbf{n}(\mathbf{r}) \approx (n_x, n_y, 1)$, the LC elastic free energy is expressed as

$$F_{\text{elastic}} = \frac{K}{2}\sum_{\mu=x,y}\int d\mathbf{r}\nabla n_\mu\cdot\nabla n_\mu. \qquad 3.$$

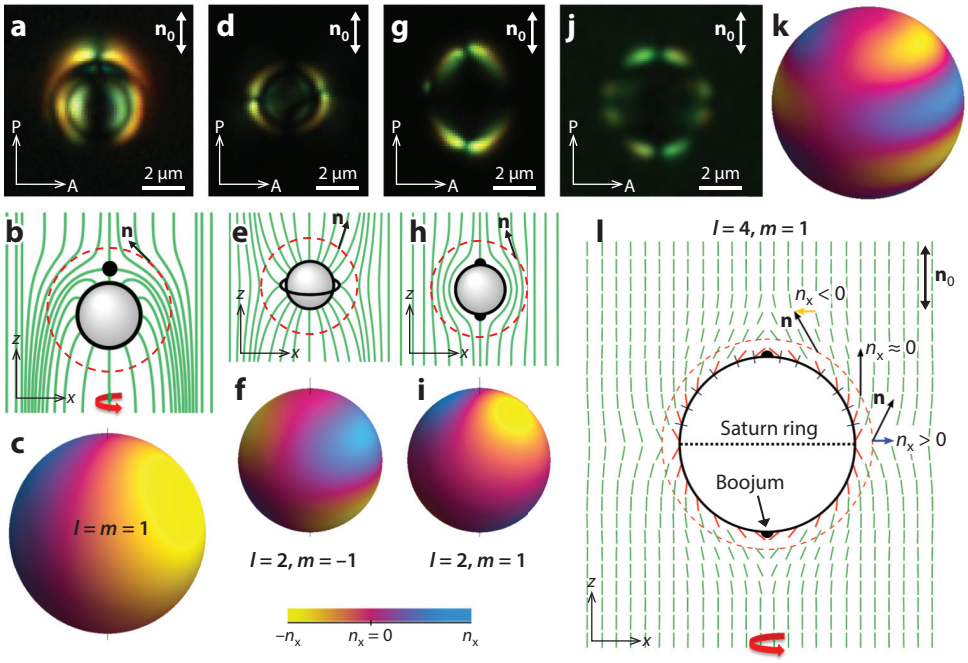

Figure 2

Elastic colloidal multipoles. (*a–c*) Elastic dipoles formed by microspheres with perpendicular boundary conditions (BCs) shown with the help of (*a*) a polarizing optical micrograph obtained between crossed polarizer P and analyzer A; (*b*) axially symmetric director configuration visualized with solid green lines (*filled black circle* depicts a hedgehog defect); and (*c*) a color-coded map of director **n** on a sphere marked with a red dashed circle in panel *b* corresponding to a dipole with indices $l = m = 1$. (*d–f*) An elastic colloidal quadrupole formed by a microsphere with perpendicular BCs shown with the help of (*d*) a polarizing optical micrograph; (*e*) axially symmetric director field **n**(**r**) visualized with green lines (*black ring* depicts a disclination); and (*f*) a color-coded map of **n** on a surrounding sphere corresponding to a quadrupole with $l = 2, m = -1$. (*g–i*) An elastic colloidal quadrupole formed by a microsphere with tangential BCs shown with the help of (*g*) a polarizing optical micrograph; (*h*) axially symmetric **n**(**r**) visualized by green lines (*black hemispheres* depict boojums); and (*i*) a color-coded map of **n** corresponding to a quadrupole with $l = 2, m = 1$. (*j–l*) An elastic colloidal hexadecapole formed by a microsphere with tilted, conically degenerate BCs shown with the help of (*j*) a polarizing optical micrograph; (*k*) a color-coded map of **n** corresponding to a multipole with $l = 4, m = 1$; and (*l*) an axially symmetric **n**(**r**) depicted with green rods (*dashed black line* at equator depicts a disclination loop; *solid black hemispheres* depict boojums). For more details, see Reference 24.

The corresponding Euler–Lagrange equations arising from the minimization of F_{elastic} are of the Laplace type, $\Delta n_\mu = 0$, with solutions expanded into multipoles:

$$n_\mu(\mathbf{r}) = \sum_{l=1}^{N} a_l (-1)^l \partial_\mu \partial_z^{l-1} \frac{1}{r}, \qquad 4.$$

where $a_l = b_l {r_0}^{l+1}$ is the elastic multipole moment of the lth order (2^l-pole), r_0 is the particle's radius, and expansion coefficients b_l can be found from experiments (24, 25). This electrostatics analogy provides a framework for understanding, predicting, and engineering both the structure of the director and self-assembly of nematic colloids.

Hedgehog point defect: a localized pointlike singularity in **n** in the bulk of LC

At no external fields, the lowest-order elastic multipoles are dipoles (2, 13), such as the ones formed by a colloidal microsphere with perpendicular BCs and a bulk hedgehog point defect

Disclination: a discontinuity in the orientational order in the form of a line defect along which **n** cannot be defined

Boojum: a localized pointlike singularity at the surface of LC

(**Figures 1*e*** and **2*a–c***). This particle-induced dipolar structure of **n**(**r**) (**Figure 2*a–c***) is invariant with respect to rotations around $\mathbf{n}_0$ but lacks mirror symmetry with respect to a plane passing through the particle's equator orthogonally to $\mathbf{n}_0$. Microspheres with perpendicular BCs can also induce a disclination loop defect around the particle's equator, often called Saturn ring, which yields an elastic quadrupole (**Figure 2*d–f***). In contrast to the elastic dipoles, this quadrupolar **n**(**r**) structure (**Figure 2*e***) is mirror symmetric with respect to the plane passing through the particle's equator orthogonally to $\mathbf{n}_0$. Colloidal spheres with strong tangential anchoring at their surface also form **n**(**r**) distortions of quadrupolar type (**Figure 2*g–i***). They induce two boojums at the poles along $\mathbf{n}_0$. For weak surface anchoring BCs or particle diameters comparable to or smaller than ξ_e, both the tangential and perpendicular BCs lead to quadrupolar configurations, similar to the elastic quadrupole with the Saturn ring or boojums, but the defects become virtual (25, 26) (within a particle's volume), as the director is allowed to deviate away from the easy-axis orientations. Particles with tilted, conically degenerate BCs (**Figure 2*j–l***) locally distort **n**(**r**), so that the polarizing optical micrographs (**Figure 2*j***) feature eight bright lobes around the particle, separated by eight dark regions within which **n**(**r**) at the particle's perimeter is parallel to $\mathbf{n}_0$. These features of polarizing micrographs are different from the cases of dipoles and quadrupoles, which exhibit alternation of two bright and two dark regions (**Figure 2*a***) and four bright and four dark regions (**Figure 2*d*,*g***), respectively. The tilt of **n**(**r**) away from $\mathbf{n}_0$ switches between clockwise and counterclockwise directions eight times as one circumnavigates the hexadecapole (**Figure 2*l***), which is different from what occurs in dipoles, where it switches two times, and quadrupoles, where it switches four times. Both the surface boojums at the particle's poles along $\mathbf{n}_0$ and the Saturn ring at the particle's equator are induced by hexadecapoles (24). To minimize the free energy cost of bulk elastic distortions, interaction of conically degenerate BCs on the microsphere with the uniform $\mathbf{n}_0$ lifts the conical degeneracy of surface anchoring and yields an axially symmetric **n**(**r**) that can be thought of as a superposition of the quadrupolar structures with boojums and the Saturn ring (**Figure 2*l***) (24).

To illustrate the analogies between elastic and electrostatic multipoles, a projection n_x of **n**(**r**) onto the x-axis orthogonal to $\mathbf{n}_0$ can be visualized using colors that highlight positive, near-zero, and negative n_x (**Figure 2*c*,*f*,*i*,*k***). Away from the particle surface and from singularities such as boojums, hedgehogs, and disclination loops, **n**(**r**) is continuous (24). The maps of n_x, plotted on spherical surfaces encompassing particles and defects, clearly illustrate the multipolar nature of elastic distortions, similar to what is observed in the electrostatic analogs (19). The color presentations of elastic distortions induced by colloidal dipoles (**Figure 2*c***), two different quadrupoles (**Figure 2*f*,*i***), and hexadecapoles (**Figure 2*k***) resemble the corresponding dipolar, quadrupolar, and hexadecapolar electrostatic charge distributions described by $\sigma_l^m(\theta, \phi) = A\cos(m\phi)P_l^m(\cos\theta)$ with $(l, m) = (1, 1), (2, \pm 1)$ and $(4, 1)$, respectively, where $-l \leq m \leq l$, A is a normalization constant, θ is a polar angle and ϕ is an azimuthal angle, and $P_l^m(\cos\theta)$ is the associated Legendre polynomial. Similar to electrostatic charge distributions, the odd moments vanish when **n**(**r**) is symmetric about the particle center, as in the cases of elastic quadrupoles and hexadecapoles presented in **Figure 2*e*,*h*,*l*** (which have coefficients b_1, b_3, and b_5 and so on equal to zero, as required by symmetry). However, both odd and even moments are present for particles with asymmetric **n**(**r**), such as elastic dipoles, for which all b_l can be nonzero (13, 21–24). The design of elastic colloidal multipoles not only takes advantage of symmetry considerations but also builds on the versatile means of controlling **n**(**r**) using shape and BCs, so that the coefficients b_l corresponding to lower-order multipoles can be tuned to be close to zero, yielding higher-order multipoles. For example, the hexadecapole shown in **Figure 2*j–l*** was designed by tuning b_2 to be close to zero while precluding the dipole and octupole moments on the basis of symmetry, as discussed above (24). In a similar way, an elastic octupole could potentially be obtained by tuning b_1 and b_2 to zero

while maximizing b_3, though this has not been achieved so far. Although it is widely assumed that elastic monopoles cannot be realized without external torques applied to colloidal particles (18), certain particles can effectively behave as elastic monopoles when they are attached to surfaces and are exerting torques on the LC director through surface anchoring (23). Both elastic monopoles and octupoles require further study.

4. COLLOIDAL INTERACTIONS MEDIATED BY ORIENTATIONAL ELASTICITY OF LIQUID CRYSTALS

The analogy between electrostatic and elastic multipoles may help in devising approaches for self-assembly of mesostructured colloidal composite materials. The potential energy of elastic interaction between nematic colloidal multipoles, which arises from the changes in free energy (which the medium tends to minimize) that result from superposition of elastic distortions induced by interacting particles, is also analogous to the energy of interaction between electrostatic multipoles (2, 13, 21, 24). For example, the potential energy of interaction between two nematic colloidal hexadecapoles scales as $P_8(\cos\theta)/R^9$ (24), that between two quadrupoles as $P_4(\cos\theta)/R^5$ (8–13, 20–22), that between two octupoles as $P_6(\cos\theta)/R^7$ (24, 25), and that between two dipoles as $P_2(\cos\theta)/R^3$ (2, 13), where $P_{2l}(\cos\theta)$ are Legendre polynomials and R is the center-to-center separation distance. Mixed interactions between elastic multipoles of different order can also be predicted by exploiting the electrostatic analogy and scale, for example, as $P_6(\cos\theta)/R^7$ between quadrupoles and hexadecapoles. Experimentally, colloidal interactions can be probed using a combination of laser tweezers and video microscopy, as shown for the case of hexadecapoles in **Figure 3**. Interaction between two nematic colloidal hexadecapoles (24) is predicted to have eight angular sectors of attraction and eight sectors of repulsion as the center-to-center separation vector **R** is rotated (**Figure 3*a*,*b***) by 2π with respect to $\mathbf{n}_0$, which is indeed observed by releasing particles from laser traps and directly visualizing the directionality of interaction forces with video microscopy (**Figure 3*c***). Tracking the motion of particles as they interact reveals that the experimental time dependencies of R and distance dependencies of interaction potential (**Figure 3*d***) at different orientations of **R** are all consistent with the model (24). Similar characterization of pair interactions was also done for elastic dipoles and quadrupoles, leaving no doubts that multipolar expansion can provide the necessary foundation for understanding the physics of nematic colloids (2, 12, 27–33). However, only some of the elastic multipoles are widely studied (the most common ones are shown in **Figure 2**); the others often require particles with nonspherical shapes or patterned surface BCs. For example, elastic dipoles with moments orthogonal to $\mathbf{n}_0$ could be induced by triangular and pentagonal platelets but so far have not been realized with microspheres (28). The description of structure and interactions between nematic colloidal particles using Legendre polynomials P_l^m or spherical harmonics with indices (l, m), where $-l \leq m \leq l$, also resembles the description of atomic orbitals of elements in the periodic table (**Figure 3*e***), where the analogous indices (l, m) are quantum numbers. Therefore, the multipolar analysis of nematic colloids not only brings about many interesting analogies and helps us to assess the diversity of structures that can be realized but also is of interest from the standpoint of the colloidal atom paradigm (3–5), as discussed next in Section 5.

5. NEMATIC COLLOIDAL ATOM PARADIGM AND COLLOIDAL CRYSTALS

Since the works of Einstein and Perrin showed how particles in colloidal dispersions obey the same statistical thermodynamics as atoms, the colloid–atom analogy has provided insights into the physics of atomic and molecular systems by enabling investigators to probe the dynamics

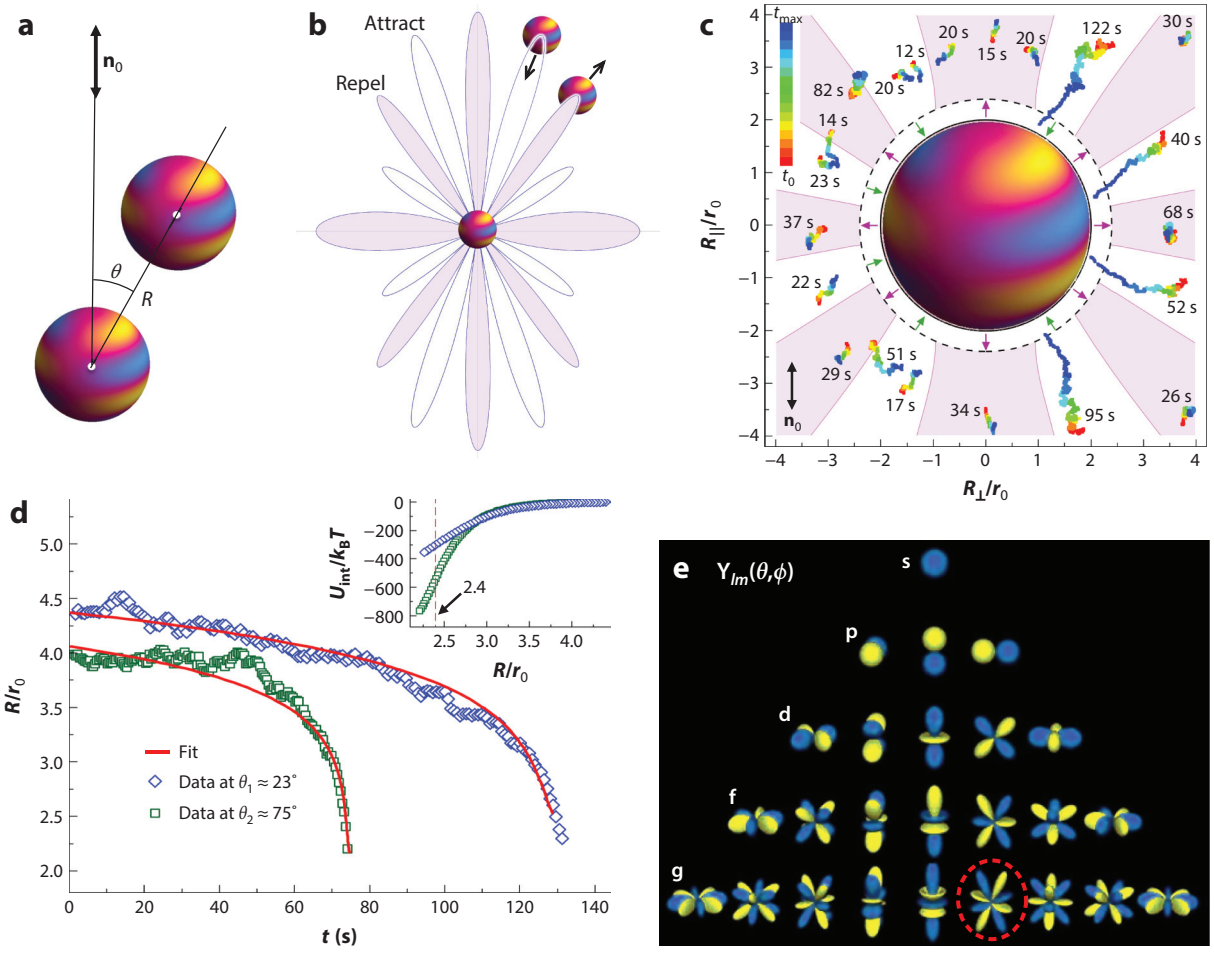

Figure 3

Colloidal interactions and analogy with chemical elements. (*a*) Definition of the angle θ between the center-to-center separation vector **R** connecting two colloidal hexadecapoles and the far-field director $\mathbf{n}_0$. (*b*) A theoretical prediction for the angular sectors of attraction (*white*) and repulsion (*magenta*) between a pair of hexadecapoles. (*c*) Experimental test of interactions indeed exhibits eight angular sectors of attraction and eight sectors of repulsion. When released from laser tweezers, hexadecapoles move toward or away from one another depending on θ, as shown by color-coding time (t) within the particle motion trajectories; the elapsed time corresponding to the time-coded trajectories is provided in seconds (s) next to these trajectories. (*d*) Time dependencies $R(t)$ for the initial θ within the attractive sectors and the dependence of interparticle pair potential U_{int} on separation R normalized by particle radius r_0 (*inset*) are consistent with the theoretical predictions. For more details, see Reference 24. (*e*) Electron probability distributions characterizing the atomic orbitals described in terms of spherical harmonics Y_{lm} with the corresponding indices as quantum numbers; the g shell configuration with $l = 4, m = 1$ of so-far-undiscovered chemical elements that are predicted to have such shells filled is marked by a dashed red circle and is analogous to a nematic colloidal hexadecapole (**Figure 2*j–l***).

of colloidal crystals and glasses (5). This colloidal atom paradigm has inspired the development of colloidal self-assembly to reproduce or exceed the diversity of atomic systems (3, 33–35). LC colloids have several advantages in addressing these grand scientific and engineering challenges. The LC host naturally allows for the realization of anisotropic interparticle interactions (2), including spontaneous alignment of shape-anisotropic particles on the basis of surface anchoring

interactions (28, 33) and exploitation of the rich multipolar behavior of elastic interaction forces (2), which would be difficult or impossible to achieve in conventional isotropic fluids (3). Furthermore, arrays of topological defect lines within the ground-state blue and cholesteric phases, or in other LC phases when stabilized by confinement, can be used to entangle or entrap colloidal particles to form various sparse crystals, quasicrystals, and other assemblies (34, 36–41). In conventional colloidal dispersions, high-symmetry crystals with 3D cubic and 2D hexagonal lattices have been studied extensively (3–7, 42), confirming and extending Einstein's colloidal atom analogy by giving direct experimental confirmations of theoretical models originally developed for atomic and molecular crystals (3, 5). However, experimental realization of colloidal architectures with low crystallographic symmetry remained challenging, even though colloids are amenable to designed control of their self-assembly through DNA functionalization (35). A series of self-assembled 2D and tetragonal 3D crystal lattices and other colloidal architectures have been achieved in LC colloidal crystals through the use of guided assembly with laser tweezers (42–48), though these colloidal superstructures could be built only particle by particle and only up to several primitive cells in dimension because of the reliance on laser tweezers rather than self-assembly alone. However, it was recently shown that low-symmetry triclinic colloidal crystals can self-assemble in LC dispersions as a result of competition between the highly anisotropic elastic interactions discussed above and (more conventional) electrostatic repulsive forces (33, 43). Realization of such triclinic colloidal crystals suggests that the high crystallographic diversity previously established for atomic and molecular crystals is now accessible in LC colloids as well.

The triclinic colloidal crystal serves as an illustration of how competition of long-range electrostatic and anisotropic quadrupolar elastic interactions in nematic colloids can lead to self-assembly of colloidal particles with long-range orientational and positional ordering (**Figure 4**) (33). The long-range electrostatic repulsions arise from weakly screened Coulomb-type forces in a low-ionic-strength nonpolar LC with a large (typically $\geq$500 nm) Debye screening length. Because the elasticity-mediated interactions are also long range, colloidal crystal assemblies with micrometer-range lattices emerging from the competition of these electrostatic and elastic forces can be an order of magnitude larger than the size of constituent colloidal particles (**Figure 4*a–d***) (33). The crystallographic axes of the triclinic lattices and the colloidal nanorods within them tend to follow the director, which can be controlled on large scales via approaches used to manufacture LC displays (18). Triclinic crystallization of particles at packing factors $\ll$1% shows potential for fabricating mesostructured composites through self-assembly on device scales, tuned by weak external stimuli, such as low voltages (43). From a fundamental science standpoint, it is interesting that the thermal fluctuations of particles within the lattice and the melting and crystallization transitions (**Figure 4*e,f***) are consistent with what is expected for their atomic counterparts (33). Mean square displacement (MSD) exhibited by colloidal particles within these dispersions saturates with time when in a crystal but continues growing when in a colloidal fluid state (inset of **Figure 4*f***). Characterization of MSD $\langle \Delta r^2(t) \rangle$ relative to the crystal lattice, quantified by the dependence of the Lindemann criterion parameter $\delta L = [3\langle \Delta r^2(t \to \infty) \rangle / (4R^2)]^{1/2}$ on the nanorod number density ρ_N, provides a means of demonstrating how low-symmetry positional ordering (**Figure 4*f***) emerges from the interplay of weakly screened electrostatic and elasticity-mediated interactions in a nematic host. The triclinic pinacoidal lattices of orientationally ordered nanorods (**Figure 4**) are the lowest-symmetry 3D colloidal crystals achieved so far (**Figure 4*a–e***) and may prompt the realization of LC colloidal architectures with other symmetries, ranging from cubic to triclinic pedial lattices.

Though so far demonstrated only for elastic quadrupoles and electrostatic monopoles, the use of competition of elastic, electrostatic, and other (e.g., magnetic) interactions to guide symmetry and density of colloidal crystals can be extended to other nematic colloidal multipoles, such as

Cholesteric phase: LC fluid locally similar to the nematic phase, but with **n** continuously rotating around an axis called the helical axis

Mean square displacement (MSD): time-average squared displacement of a particle, a measure of the deviation of its position from some reference position

Lindemann criterion: melting of crystals occurs because of vibrational instability, when the amplitude of thermal vibrations of building blocks is high compared with distances between them

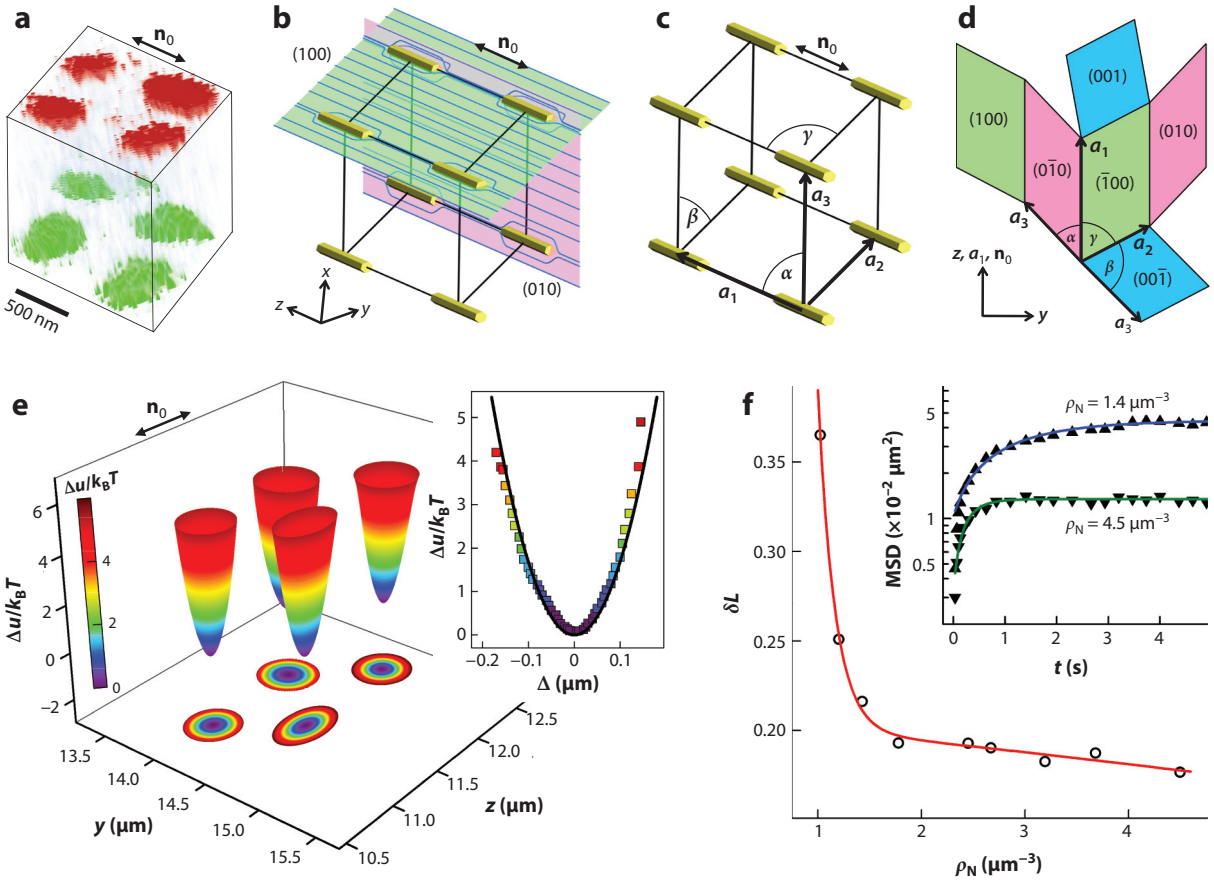

Figure 4

Colloidal crystals. (*a*) 3D micrograph showing a primitive unit cell of a triclinic colloidal crystal, which was reconstructed on the basis of confocal imaging. It shows spatial arrangements of colloidal particles as they explore the potential energy landscape near their minimum-energy triclinic lattice sites. (*b–d*) Schematics (not to scale) of a primitive cell of a triclinic colloidal crystal, (*b*) showing the director field $\mathbf{n}(\mathbf{r})$ distortions (*blue lines*) induced by nanorods in the background of the uniform far-field director $\mathbf{n}_0$, (*c*) defining parameters of a triclinic lattice, and (*d*) showing it unfolded. Crystallographic planes, axes, and angles are marked on the schematics. (*e*) The potential energy Δu landscape corresponding to four lattice sites in the (100) crystallographic plane of a triclinic crystal. The inset shows a local distance Δ dependence of the relative Δu experienced by colloidal particles. (*f*) Lindemann parameter δL versus ρ_N of nanorods, characterizing the crystallization–melting transition. Inset shows the mean square displacement (MSD) of particles versus time at $\rho_N = 1.4\ \mu m^{-3}$ (▲) and $4.5\ \mu m^{-3}$ (▼). For more details, see Reference 33.

dipoles and hexadecapoles (**Figure 2**), which for the most part were previously exploited only from the standpoint of interactions guided by laser tweezers (24, 44–48). Considering the intrinsic anisotropy and diversity of elastic multipoles, one can expect a large variety of low-symmetry colloidal architectures emerging from such interactions. Furthermore, because atomic orbitals and the outermost occupied electron shells of chemical elements (**Figure 3*e***) are described by spherical harmonics $Y_{lm}(\theta, \phi)$, they are analogous (in terms of symmetry) to the nematic colloidal atoms. Because the symmetry of the director wiggle wave function of nematic hexadecapolar colloids (**Figure 2*k*,*l***) would correspond to chemical elements with filled g shells (**Figure 3*e***),

which have not been discovered, nematic colloidal atoms already exceed the diversity of their atomic counterparts (24).

6. MOLECULAR-COLLOIDAL ANISOTROPIC FLUIDS

Magnetic hysteresis: a characteristic of ferromagnets associated with the lack of retraceability of the magnetization curve when the magnetic field is relaxed

The realization of thermodynamic phases that combine low-symmetry order and fluidity is one of the grand challenges in soft matter research. Both molecular and conventional colloidal LCs are classic examples of how various degrees of orientational and partial positional order can be combined with fluidity in nematic, smectic, and columnar phases (18), though they tend to be nonpolar and they exhibit high symmetry. Starting from the early work of Brochard & de Gennes (49), researchers predicted and demonstrated self-alignment of shape-anisotropic colloidal particles such as rods and platelets in LCs (28, 33, 36, 50–56). This LC-mediated spontaneous orientation of anisotropic particles relative to $\mathbf{n}_0$ emerges from elastic (49, 55) and/or surface anchoring–based (56) interactions. It allows the system-minimizing surface anchoring energy at the LC–colloidal interface given by Equation 1 or elastic energy due to the bulk distortions near the particle-induced BCs at its surface given by Equation 2, though surface anchoring and elastic energies are often comparable and both contribute to defining particle orientations (57–68). In most cases, dilute dispersions of anisotropic colloidal particles in LCs do not alter the symmetry of the LC dispersion as compared to that of the LC, as the orientations of particles typically simply mimic the ordering of the LC host (69) and can be treated in terms of the behavior of individual inclusions (70–88). LC–colloidal interactions, along with the direct magnetic interparticle interactions, can also lead to the polar alignment of magnetic colloidal inclusions (49–54), although the orientations of the magnetic dipoles of colloidal particles are commonly slaved to $\mathbf{n}$, orienting either parallel or perpendicular to it without breaking uniaxial symmetry. Experimental realization of low-symmetry ordered fluids, such as orthorhombic biaxial LCs (89), is challenging for both molecular and colloidal systems, especially in the case of nematic phases without positional ordering. However, similar to the case of low-symmetry colloidal crystals (33), LC colloidal dispersions of various nanoparticles also provide a series of advantages and promise realization of hybrid LC–colloidal fluids with low-symmetry orientational order (16). For example, a recently introduced molecular-colloidal complex fluid formed by a dispersion of magnetic nanoplates in a thermotropic nematic LC exhibits coexisting polar and biaxial ordering of organic molecular and magnetic colloidal building blocks, with the lowest C_s symmetry orientational order in a fluid medium, which so far has not been realizable in purely molecular or colloidal systems (16).

In the molecular-colloidal LC with the C_s symmetry, guided by interactions at different length scales (16), rodlike organic molecules of the host fluid spontaneously orient along the director, whereas magnetic colloidal nanoplates order with their dipole moments $\mathbf{m}$ (**Figure 5*a–d***) parallel to each other, but pointing at an angle to the director, yielding macroscopic magnetization at no external fields (**Figure 5*e,f***). This unusual physical behavior is enabled by the control of conically degenerate surface anchoring at the magnetic nanoparticle surfaces (16, 17), which assures tilted orientations of magnetic moments $\mathbf{m}$ and magnetization $\mathbf{M}$ with respect to $\mathbf{n}_0$. Magnetic hysteresis loops (**Figure 5*e,f***) and facile switching of such ordered ferromagnetic fluids emerge from the competing actions of elastic and magnetic torques and a rich magnetic domain structure (16). This and other molecular-colloidal complex LC fluids promise rich behavior arising from the properties of solid nanoparticles and their long-range ordering prompted by interactions with a host medium at the mesoscale. Future research may lead to hybrid molecular-colloidal soft matter phases with different point group symmetries describing the order of molecular and colloidal building blocks, such as an orthorhombic biaxial (89) nematic molecular-colloidal fluid in which anisotropic nanoparticles (such as nanorods) could orientationally order in a direction orthogonal

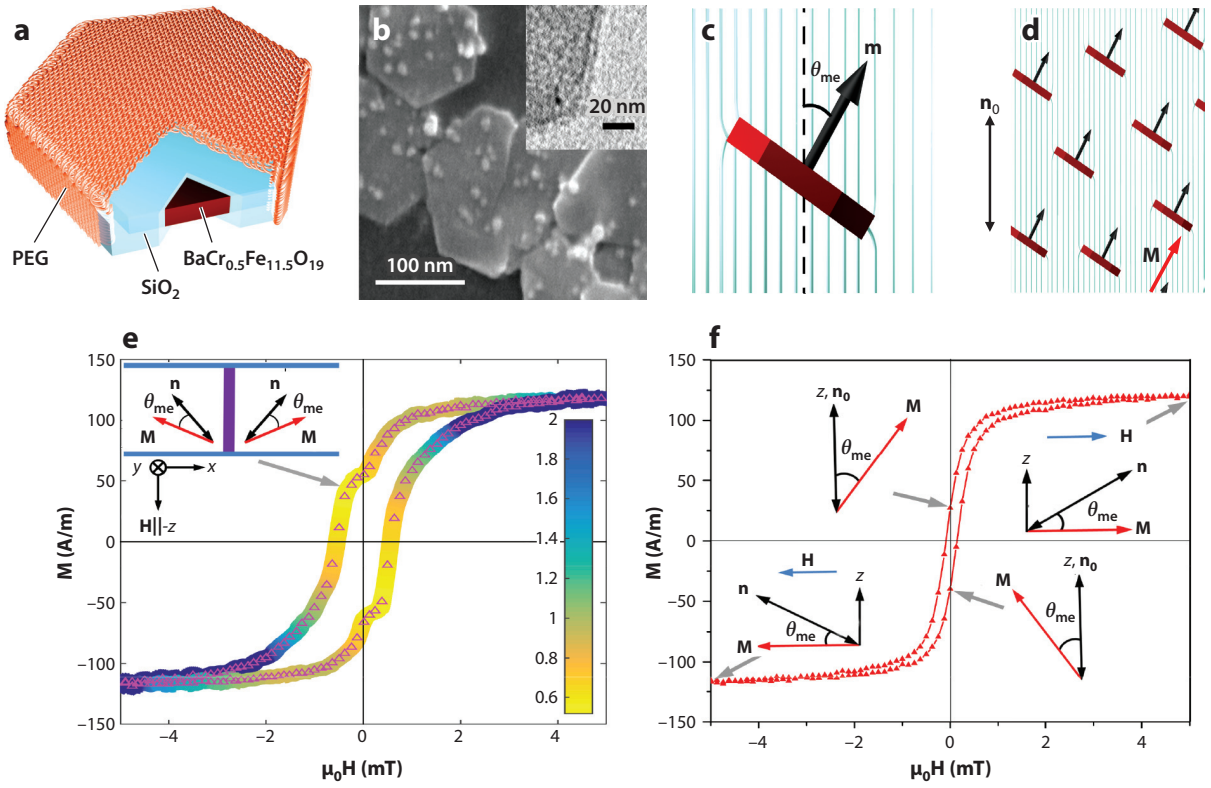

Figure 5

Molecular-colloidal liquid crystal (LC) fluids. (*a*) Schematic of a ferromagnetic nanoplate, coated with silica and then further functionalized with polyethylene glycol (PEG). (*b*) Scanning transmission electron microscopy (TEM) image of such magnetic nanoplates, with a zoomed-in TEM image of a nanoplatelet's edge revealing the approximately 5-nm-thick silica shell (*inset*). (*c*) Schematic of an individual nanoplate in LC, with the magnetic moment **m** tilted away from the far-field director $\mathbf{n}_0$ to an angle θ_{me}. (*d*) A schematic of the biaxial ferromagnetic molecular-colloidal hybrid LC with magnetization **M** tilted away from $\mathbf{n}_0$. (*e*) Experimental (*open triangle symbols*) and theoretical (*solid curve*, with the relative domain size coded according to the color scheme shown on the right side of the panel, where the average ratio of lateral size of domains to cell thickness varies from 0.5 to 2) magnetic hysteresis loop measured for magnetic field along $\mathbf{n}_0$. Schematics in the top-left inset show relative orientations of **M** and the director **n** within domains that correspond to the part of the hysteresis loop indicated by a gray arrow. (*f*) Hysteresis loop probed for the same sample as in panel *e*, but for magnetic field $\mathbf{H} \perp \mathbf{n}_0$; relative orientations of **M** and **n** corresponding to different parts of the hysteresis loop are indicated by gray arrows. For more details, see Reference 16.

to the ordering direction of rodlike LC molecules. Such hybrid molecular-colloidal systems, in which colloidal self-organization is enriched by elastic and surface anchoring interactions, are expected to yield soft condensed matter phases that could not be realized previously.

7. TOPOLOGY, GEOMETRY, AND CHIRALITY: SURFACES WITH AND WITHOUT BOUNDARIES

The interaction of colloidal particles with the LC director field can be understood and generalized on the basis of the interplay between the topologies of fields and surfaces widely studied by mathematicians (90). All surfaces are characterized (up to homeomorphism) by their genus, orientability, and number of boundary components, as stated by the classification theorem (90).

Colloidal particles with all dimensions larger than $\xi_e = K/W$ produce well-defined BCs and can be considered as having orientable surfaces without boundaries, so that their interaction with the $\mathbf{n}(\mathbf{r})$ depends on the particle surface's genus g (or, equivalently, its Euler characteristic $\chi = 2 - 2g$). Colloidal particles tend to have surfaces with spherical or other topologically simple shapes with $g = 0$ and $\chi = 2$, such as prisms (continuously deformable to spheres). However, one can fabricate colloidal particles with different numbers of handles and $g \neq 0$ (91–95). Fabrication approaches include conventional photolithography (28), direct laser writing (91, 92), two-photon polymerization (93, 94), and laser-induced reduction of colloidal graphene oxide nanoflakes (95). In LCs, these particles induce 3D $\mathbf{n}(\mathbf{r})$ and topological defects dictated by colloidal topology. 3D nonlinear optical imaging and numerical modeling (91–94) reveal that topological charge induced by the particles is conserved and that the net hedgehog charge m of particle-induced bulk defects obeys predictions of the Gauss–Bonnet and Poincaré–Hopf index theorems. Although particles can induce different $\mathbf{n}(\mathbf{r})$ structures, depending on confinement, external fields, and material properties, the sum of hedgehog charges due to induced point defects and disclination loops, $\sum_i m_i = -m_c = \pm\chi/2$, always compensates for the colloidal particles' hedgehog charge m_c due to $\mathbf{n}(\mathbf{r})$ at their surfaces and is uniquely predetermined by the particles' topologies (**Figure 6**). The use of a plus or a minus sign in this relation depends on the choice of the vectorizing $\mathbf{n}(\mathbf{r})$-field direction, but the relative signs of the induced defects are fixed. This relation allowed the establishment of a procedure for the assignment and summation of topological charges in 3D director fields (91).

Particles with tangential BCs additionally induce boojums at the LC–colloidal interface. The total boojum winding number in the projection of $\mathbf{n}(\mathbf{r})$ to the particle surface, $\mathbf{n}_s(\mathbf{r})$, is always $\Sigma_i s_i = \chi$, also satisfying topological theorems (92). These simple relations describe defects induced both by the $g = 0$ spherical surfaces (**Figures 1** and **2**) and by surfaces such as handlebodies and torus knots with $g \neq 0$ (**Figure 6**), though additional self-compensating defects can appear to reduce the energetic cost of elastic distortions associated with matching BCs on colloidal surfaces to $\mathbf{n}_0$. For example, $\Sigma_i s_i = 0$ for self-compensating boojums induced by a trefoil knot colloidal particle (**Figure 6*g–i***), as expected for the torus knot's surface with $\chi = 0$. However, beyond the predictions of topological theorems, nematic colloids can also have mutually tangled physical knots of particles and line defects in $\mathbf{n}(\mathbf{r})$, as illustrated in **Figure 6*j–l*** (93). For all nematic colloidal particles, the interplay of topologies of surfaces, fields, and defects guides $\mathbf{n}(\mathbf{r})$ to comply with the particle shape, generating knotted, linked, and other 3D configurations (91–94) and thereby providing experimental insights into aspects of mathematical knot theory (90, 93, 94).

Nematic colloidal particles in the form of thin foil with two lateral dimensions $\gg \xi_e$ but one dimension (thickness) $\ll \xi_e$ behave as analogs of orientable surfaces with boundaries, to which the constraints on induced defects discussed above cannot apply and, generally, no defects need to be induced (91, 96). Yet, by morphing the shapes of such foil-based particles, one can pattern the defects to achieve various elastic multipoles and drive LC-mediated self-assembly similar to that exhibited by nematic colloidal particles with surfaces without boundaries (96). Their behavior is different from that of both microparticles (larger than ξ_e) with strong BCs (**Figures 1*d*,*e***, **2**, and **3**) and nanoparticles (smaller than ξ_e) with effectively weak surface anchoring (**Figures 4** and **5**), being capable of inducing no defects or various self-compensating defect structures depending on their geometric shape and orientation relative to $\mathbf{n}_0$ (96). Nonorientable colloidal particles with boundaries have also been recently theoretically considered (97), though their experimental realization still presents a challenge.

The shape of colloidal particles plays a key role in defining the locations and types of induced defects even when the topology of particle surfaces stays simple (**Figure 7**). For example, by shaping $g = 0$ colloidal particles with perpendicular BCs as truncated pyramids (**Figure 7*a–d***), one preselects the topology-complying defect with $m = \pm 1$ to take the form of a half-integer

Genus (g): a maximum integer number of cuttings along nonintersecting closed simple curves that do not render the resultant manifold disconnected, equal to the number of handles on it

Euler characteristic (χ): a topological invariant $\chi = 2 - 2g$ that describes a topological space's shape or structure regardless of the way it is bent

Hedgehog charge: degree of $\mathbf{n}$ along S, of space V bounded by a $S = \partial V$, calculated by integrating the Jacobian of $\mathbf{n}(\mathbf{r})$, $m = (1/4\pi)\int_S dx_1 dx_2 \mathbf{n} \cdot \partial_1\mathbf{n} \times \partial_2\mathbf{n}$

Boojum winding number: the number of times that the director $\mathbf{n}_s$ at the LC–particle interface rotates by 2π as one circumnavigates the surface boojum's defect core once

Handlebody: a submanifold of Euclidean space comprising a ball with handles attached to it along its boundary

Trefoil knot: the simplest nontrivial knot obtained by joining together the two loose ends of a common overhand knot, yielding a knotted loop

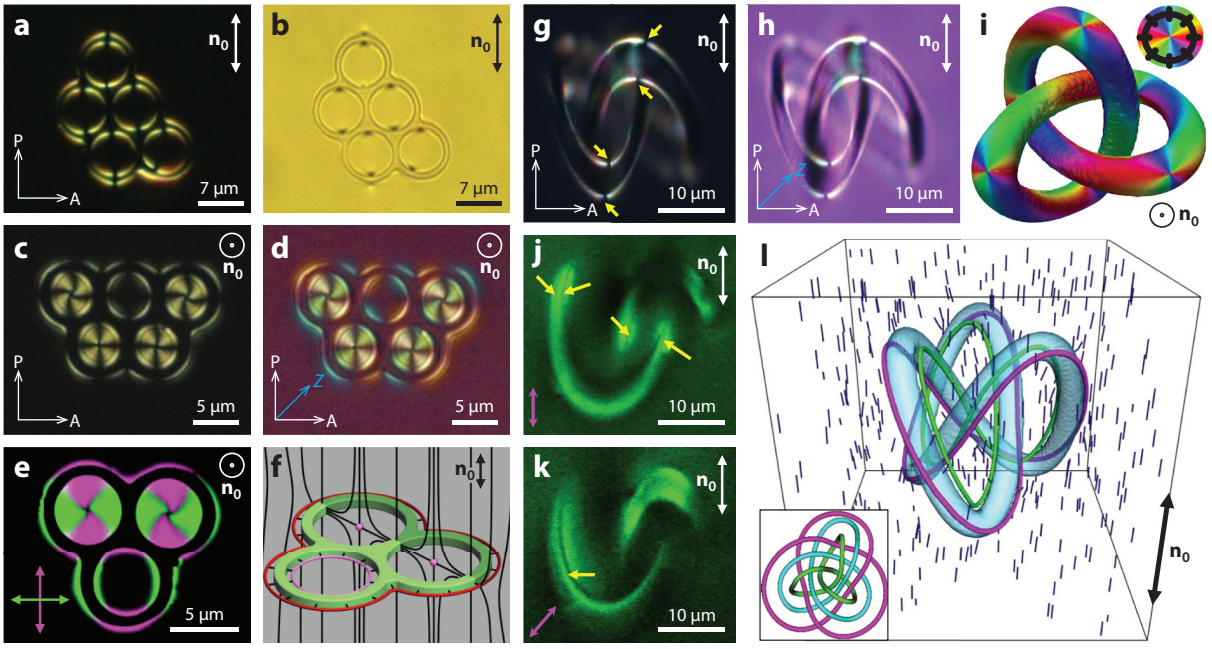

Figure 6

Topology-controlled nematic colloidal behavior. (*a*,*b*) Transmission-mode optical micrographs of a genus $g = 5$ colloidal handlebody with tangential boundary conditions (BCs) in a nematic liquid crystal (LC) obtained (*a*) between crossed polarizer P and analyzer A and (*b*) without polarizers. Boojums are visible as discontinuities in bright brushes in panel *a* and as dark light-scattering localized regions in panel *b*. (*c*,*d*) Polarizing optical micrographs of a $g = 5$ colloidal handlebody with perpendicular BCs in a nematic LC obtained between crossed P and A (*c*) without and (*d*) with an additional 530-nm phase-retardation plate with the slow axis *Z* marked by a blue arrow. (*e*,*f*) A $g = 3$ colloidal handlebody with perpendicular BCs in a nematic LC (*e*) imaged using three-photon excitation fluorescence polarizing microscopy and (*f*) shown schematically. The overlaid fluorescence patterns obtained for the two mutually orthogonal polarizations (*green* and *magenta double arrows*) of excitation light are shown using green and magenta coloration. Black lines represent $\mathbf{n}(\mathbf{r})$, and the red or magenta points and rings depict topological defects with opposite hedgehog charges. (*g*–*i*) A trefoil knot particle with tangential BCs in an aligned LC imaged (*g*,*h*) between crossed P and A (*g*) without and (*h*) with an additional 530-nm retardation plate whose slow axis *Z* is marked by a blue arrow. Boojums are indicated by yellow arrows in panel *g*. (*i*) 3D representation of the director field $\mathbf{n}(\mathbf{r})$ deviating away from the far-field director $\mathbf{n}_0$ due to the incorporated trefoil knot particle. Colors depict the azimuthal orientation of $\mathbf{n}(\mathbf{r})$ when projected onto a plane orthogonal to $\mathbf{n}_0$ according to the scheme shown in the inset. The structure is visualized on a tube following the knot particle's surface. Points where different colors meet are boojums. (*j*–*l*) A colloidal trefoil knot with perpendicular BCs. (*j*,*k*) Three-photon excitation fluorescence polarizing microscopy images of $\mathbf{n}(\mathbf{r})$ for excitation light polarizations (*magenta double-headed arrows*) at different orientations with respect to $\mathbf{n}_0$. Yellow arrows mark the defect lines. (*l*) Computer-simulated $\mathbf{n}(\mathbf{r})$ around a trefoil knot with perpendicular BCs and the torus plane oriented orthogonally to $\mathbf{n}_0$. Green and magenta lines show regions with reduced scalar order parameter corresponding to the cores of two knotted defect lines (panels *j* and *k*). Inset shows a schematic of mutual linking between the particle knot (*blue*) and defect knots (*green* and *magenta*). For more details, see References 92–94.

disclination loop localized near the pyramid's base, and one uniquely defines the orientation of the ensuing elastic dipole (**Figure 7*d***). Polygonal platelets (**Figure 7*e–j***) with odd and even numbers of edge faces behave as dipoles and quadrupoles, respectively, illustrating that the elastic multipole nature can be controlled by tuning the particle's geometric shape (28). Particles shaped as letters of the Latin alphabet (**Figure 7*k*,*l***), on the other hand, exhibit well-defined orientations with respect to $\mathbf{n}_0$ and induce surface boojums with $\Sigma_i s_i = \chi$ correlated with their shapes. Other colloidal shapes studied recently include pyramids, spirals, shape-morphing elastomeric rods, gourd-shaped dimers, particles with nanoscale surface roughness, and so on (98–113), in all cases demonstrating that the geometric shape predefines the locations of topological defects and colloidal interactions.

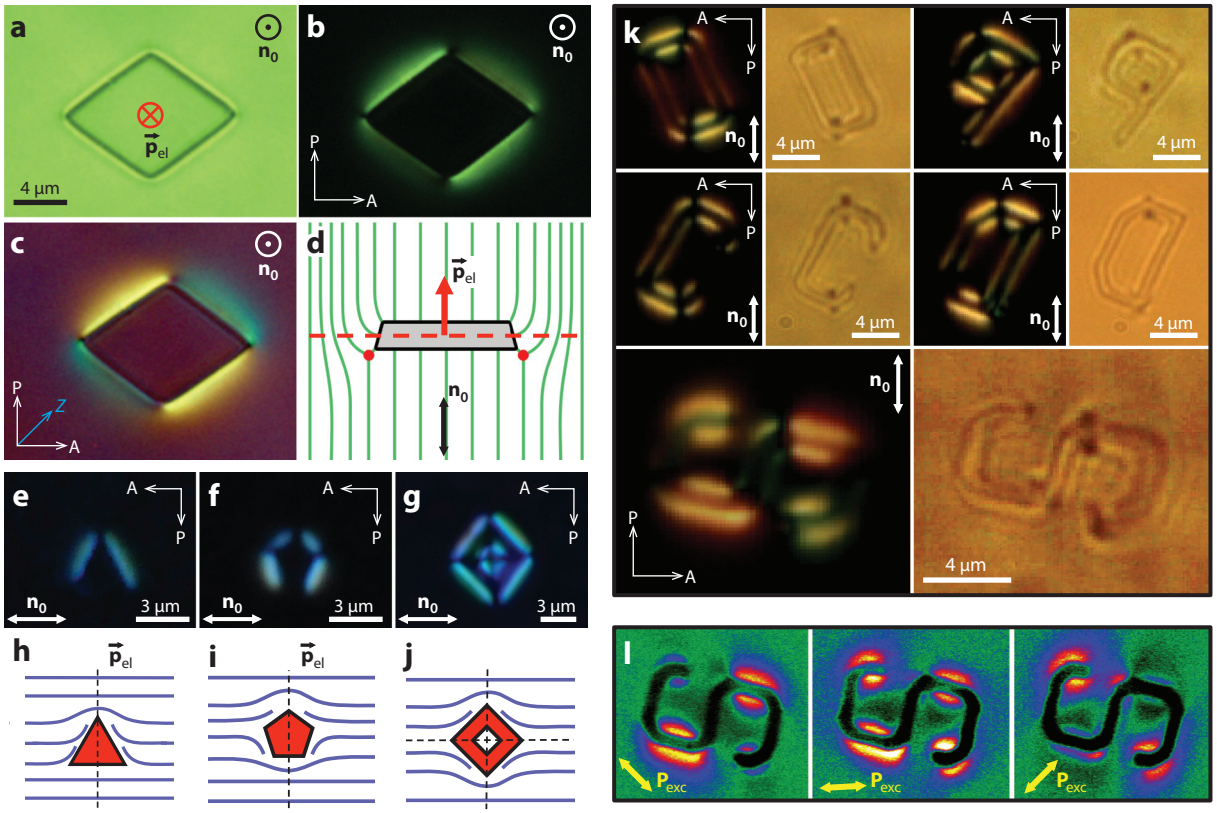

Figure 7

Shape-controlled nematic colloidal behavior. (*a–c*) A truncated pyramid with a rhomb-like base imaged by using optical microscopy (*a*) without polarizers, (*b*) between crossed polarizer P and analyzer A, and (*c*) with a 530-nm phase-retardation plate (with the slow axis *Z* marked by a blue arrow). (*d*) Director field $\mathbf{n}(\mathbf{r})$ (*green lines*) around the particle in a cross-section plane containing $\mathbf{n}_0$; red filled circles indicate the intersections of a disclination loop with the plane. The red arrow shows the elastic dipole $\mathbf{p}_{el}$. (*e–g*) Polarizing optical micrographs of $\mathbf{n}(\mathbf{r})$ induced by polygonal prisms with tangential boundary conditions and (*e*) three, (*f*) five, and (*g*) four edge faces. (*h–j*) Schematic illustrations of the respective $\mathbf{n}(\mathbf{r})$ structures (*blue lines*) around the prisms that correspond (*h*,*i*) to elastic dipoles for odd numbers of edge faces and (*j*) to elastic quadrupoles for even numbers of edge faces. (*k*) Optical micrographs of particles with the shapes of Latin alphabet letters immersed in an aligned liquid crystal and viewed between crossed polarizer P and analyzer A (*left images*) and without polarizers (*right images*); boojums are visible as discontinuities in bright brushes in the former and as dark localized regions in the latter. (*l*) Three-photon excitation fluorescence polarizing microscopy images of $\mathbf{n}(\mathbf{r})$ around the S-shaped particles obtained for linear polarizations of excitation light $\mathbf{P}_{exc}$ (*yellow double-headed arrows*). For more details, see References 28, 36, and 72.

Often closely related to particle shape and topology, chirality of nematic colloids can also play an important role in defining their physical behavior. For example, the knot-shaped particles shown in **Figure 6*g–l*** are chiral in nature and induce 3D director distortions that mimic this chirality (93, 94), similar to the surface-attached chiral particles studied in Reference 23. However, even mirror-symmetric particles can induce 3D chiral distortions of $\mathbf{n}(\mathbf{r})$ due to nontrivial conformation states and transformations of the topological defects (102). The chiral nature of LC hosts also drives formation of chiral distortions in $\mathbf{n}(\mathbf{r})$ and chiral colloidal superstructures. For example, it can lead to formation of twist-escaped disclination loops around particles (114), to formation of

sparse assemblies enabled by cholesteric quasi-layers (40), and to LC topological solitons bound to particles (115, 116) and also to other types of chirality-enabled colloidal behavior (117–126).

LC topological soliton: a nonsingular, continuous, but topologically nontrivial configuration of $\mathbf{n}(\mathbf{r})$ that cannot be transformed to a uniform state through smooth deformations of the field

Photon upconversion: a process of sequential absorption of two or more photons that leads to light emission at a wavelength shorter than that of excitation

8. PROPERTY ENGINEERING IN NEMATIC COLLOIDAL COMPOSITES

Self-organization of nanosized functional units is an exceptionally promising way of designing artificial composite materials with new macroscopic physical behavior (127). Many approaches focus on the material behavior arising from ordering, colocalization, and alignment of nanoparticles, which lead to controlled plasmon–exciton and other interactions enabled by the nanoscale confinement (127). In the field of LC colloids, recent studies explore such interactions at the levels of individual quantum dots, photon upconversion and plasmonic nanoparticles (128–138), and novel composite materials (43, 55, 56, 61, 63, 64, 66, 67, 69, 73, 80, 139–144), demonstrating a means of controlling nanoparticle and composite optical characteristics such as luminescence lifetimes. For example, plasmon–exciton interactions can alter blinking statistics of quantum dot nanoparticles and can shorten luminescence lifetimes by an order of magnitude (128). The host medium's intrinsic order translates into the self-organization of immersed inclusions depending on the shapes and/or sizes of particles and on how anisotropic colloidal structures interact with the molecular alignment fields, as discussed above. Shape-dependent colloidal interactions and ordering of quantum dots, dye-doped nanostructures, and plasmonic metal nanoparticles reveal underpinning physical mechanisms that can ultimately determine composite properties (55, 61). Facile control of nanoparticle and molecular organization and the ensuing composite properties can be achieved by applying electric, magnetic, and optical fields (80). In addition to the equilibrium structures and various crystal or LC colloidal phases, future designs of composite material behavior may also involve various types of LC colloidal dynamics (145–150), though additional studies are still needed to make this possible.

9. CONCLUSIONS AND OUTLOOK

Mimicking and ultimately exceeding the diversity of organization of atomic elements are among the main goals of colloidal science, which could allow for self-assembly of a broad range of mesostructured composite materials. Self-organization of colloidal nanometer- and micrometer-sized particles dispersed in LCs is a promising approach to achieve this goal. Due to unusual but controlled molecular interactions at colloidal surfaces, the solid particles can locally perturb the uniform molecular alignment of the nematic host, forming elastic multipolar distortions of ordering that drive highly anisotropic interactions and lead to low-symmetry organization in the form of colloidal crystals with tunable lattice parameters and colloidal fluids with orientational ordering. The interdisciplinary research on LC colloids addresses some of the most exciting problems at the interfaces of materials engineering, soft matter physics, nanoscience, and photonics. The emerging scientific frontiers at the nexus of these fields show exceptional promise for significant new discoveries and applications. They will advance our fundamental knowledge of self-assembly in complex fluids and will impinge on fields as diverse as information displays, metamaterial and photonic crystal fabrication, and energy conversion.

DISCLOSURE STATEMENT

The author is not aware of any affiliations, memberships, funding, or financial holdings that might be perceived as affecting the objectivity of this review.

ACKNOWLEDGMENTS

I gratefully acknowledge research contributions and discussions over many years with my former and current students and postdocs working on LC colloids, including P. Ackerman, M. Campbell, J. Evans, D. Gardner, J. Giller, A. Hess, L. Jiang, C. Lapointe, T. Lee, Q. Liu, A. Martinez, H. Mundoor, M. Pandey, S. Park, O. Puls, B. Senyuk, R. Trivedi, O. Trushkevych, C. Twombly, M. Varney, Y. Yuan, and Q. Zhang. I also acknowledge support from National Science Foundation grant DMR-1410735.

LITERATURE CITED

1. Chaikin PM, Lubensky TC. 2000. *Principles of Condensed Matter Physics*. Cambridge, UK: Cambridge Univ. Press
2. Poulin P, Holger S, Lubensky TC, Weitz DA. 1997. *Science* 275:1770–73
3. Manoharan VN. 2015. *Science* 349:1253751
4. Anderson VJ, Lekkerkerker HNW. 2002. *Nature* 416:811–15
5. Lekkerkerker HNW, Tuinier R. 2011. *Colloids and the Depletion Interaction*. Dordrecht, Neth.: Springer
6. Sacanna S, Irvine WTM, Chaikin PM, Pine DJ. 2010. *Nature* 464:575–78
7. Jones MR, Macfarlane RJ, Lee B, Zhang J, Young KL, et al. 2010. *Nat. Mater.* 9:913–17
8. Ruhwandl RW, Terentjev EM. 1997. *Phys. Rev. E* 55:2958–61
9. Gu Y, Abbott NL. 2000. *Phys. Rev. Lett.* 85:4719–22
10. Ramaswamy S, Nityananda R, Raghunathan VA, Prost J. 1996. *Mol. Cryst. Liq. Cryst. Sci. Technol. Sect. A* 288:175–80
11. Loudet JC, Poulin P. 2001. *Phys. Rev. Lett.* 87:165503
12. Stark H. 2001. *Phys. Rep.* 351:387–474
13. Lubensky TC, Pettey D, Currier N, Stark H. 1998. *Phys. Rev. E* 57:610–25
14. Nelson DR. 2002. *Nano Lett.* 2:1125–29
15. Lagerwall JPF, Scalia G, eds. 2016. *Liquid Crystals with Nano and Microparticles*. Singapore: World Sci.
16. Liu Q, Ackerman PJ, Lubensky TC, Smalyukh II. 2016. *PNAS* 113:10479–84
17. Ramdane OO, Auroy P, Forget S, Raspaud E, Martinot-Lagarde P, Dozov I. 2000. *Phys. Rev. Lett.* 84:3871–74
18. de Gennes PG, Prost J. 1993. *The Physics of Liquid Crystals*. New York: Oxford Univ. Press. 2nd ed.
19. Jackson JD. 1962. *Classical Electrodynamics*. New York: John Wiley & Sons
20. Pergamenshchik VM, Uzunova VA. 2011. *Phys. Rev. E* 83:021701
21. Lev BI, Chernyshuk SB, Tomchuk PM, Yokoyama H. 2002. *Phys. Rev. E* 65:021709
22. Tovkach OM, Chernyshuk SB, Lev BI. 2012. *Phys. Rev. E* 86:061703
23. Martinez A, Lee T, Asavei T, Rubinsztein-Dunlop H, Smalyukh II. 2012. *Soft Matter* 8:2432–37
24. Senyuk B, Puls O, Tovkach OM, Chernyshuk SB, Smalyukh II. 2016. *Nat. Commun.* 7:10659
25. Chernyshuk SB, Tovkach OM, Lev BI. 2014. *Phys. Rev. E* 89:032505
26. Ruhwandl RW, Terentjev EM. 1997. *Phys. Rev. E* 56:5561–65
27. Loudet JC, Barois P, Poulin P. 2000. *Nature* 407:611–13
28. Lapointe CP, Mason TG, Smalyukh II. 2009. *Science* 326:1083–86
29. Muševič I, Škarabot M, Babič D, Osterman N, Poberaj I, et al. 2004. *Phys. Rev. Lett.* 93:187801
30. Škarabot M, Ravnik M, Babič D, Osterman N, Poberaj I, et al. 2006. *Phys. Rev. E* 73:021705
31. Fukuda J, Stark H, Yoneya M, Yokoyama H. 2004. *Phys. Rev. E* 69:041706
32. Takahashi K, Ichikawa M, Kimura Y. 2008. *J. Phys. Condens. Matter* 20:075106
33. Mundoor H, Senyuk B, Smalyukh II. 2016. *Science* 352:69–73
34. Wood TA, Lintuvuori JS, Schofield AB, Marenduzzo D, Poon WCK. 2011. *Science* 334:79–83
35. Jones MR, Macfarlane RJ, Lee B, Zhang J, Young KL, et al. 2010. *Nat. Mater.* 9:913–17
36. Senyuk B, Liu Q, Bililign E, Nystrom PD, Smalyukh II. 2015. *Phys. Rev. E* 91:040501
37. Smalyukh II, Kuzmin AN, Kachynski AV, Prasad PN, Lavrentovich OD. 2005. *Appl. Phys. Lett.* 86:021913
38. Ravnik M, Alexander GP, Yeomans JM, Žumer S. 2011. *PNAS* 108:5188–92

39. Gharbi MA, Manet S, Lhermitte J, Brown S, Milette J, et al. 2016. *ACS Nano* 10:3410–15
40. Trivedi RP, Klevets II, Senyuk B, Lee B, Smalyukh II. 2012. *PNAS* 109:4744–49
41. Araki T, Tanaka H. 2006. *Phys. Rev. Lett.* 97:127801
42. Blanc C. 2016. *Science* 352:40–41
43. Mundoor H, Smalyukh II. 2015. *Small* 11:5572–80
44. Nych A, Ognysta U, Škarabot M, Ravnik M, Žumer S, Muševič I. 2013. *Nat. Commun.* 4:1489
45. Varney MCM, Zhang Q, Senyuk B, Smalyukh II. 2016. *Phys. Rev. E* 94:042709
46. Muševič I, Škarabot M, Tkalec U, Ravnik M, Žumer S. 2006. *Science* 313:954–58
47. Ognysta U, Nych A, Nazarenko V, Škarabot M, Muševič I. 2009. *Langmuir* 25:12092–100
48. Ognysta UM, Nych AB, Uzunova VA, Pergamenschik VM, Nazarenko VG, et al. 2011. *Phys. Rev. E* 83:041709
49. Brochard F, de Gennes PG. 1970. *J. Phys.* 31:691–708
50. Rault J, Cladis PE, Burger JP. 1970. *Phys. Lett. A* 32:199–200
51. Chen S-H, Amer NM. 1983. *Phys. Rev. Lett.* 51:2298–301
52. Mertelj A, Lisjak D, Drofenik M, Čopič M. 2013. *Nature* 504:237–41
53. Zhang Q, Ackerman PJ, Liu Q, Smalyukh II. 2015. *Phys. Rev. Lett.* 115:097802
54. Mertelj A, Osterman N, Lisjak D, Čopič M. 2014. *Soft Matter* 10:9065–72
55. Liu Q, Cui Y, Gardner D, Li X, He S, Smalyukh II. 2010. *Nano Lett.* 10:1347–53
56. Liu Q, Senyuk B, Tang J, Lee T, Qian J, et al. 2012. *Phys. Rev. Lett.* 109:088301
57. Hashemi SM, Ejtehadi MR. 2015. *Phys. Rev. E* 91:012503
58. Evans JS, Beier CN, Smalyukh II. 2011. *J. Appl. Phys.* 110:033535
59. Hess AJ, Liu Q, Smalyukh II. 2015. *Appl. Phys. Lett.* 107:071906
60. Silvestre NM, Tasinkevych M. 2017. *Phys. Rev. E* 95:012606
61. Jiang L, Mundoor H, Liu Q, Smalyukh II. 2016. *ACS Nano* 10:7064–72
62. Eskandari E, Silvestre NM, da Gama MMT, Ejtehadi MR. 2014. *Soft Matter* 10:9681–87
63. Sheetah GH, Liu Q, Smalyukh II. 2016. *Opt. Lett.* 41:4899–902
64. Zhang Y, Liu Q, Mundoor H, Yuan Y, Smalyukh II. 2015. *ACS Nano* 9:3097–108
65. Sengupta A, Herminghaus S, Bahr C. 2011. *Mol. Cryst. Liq. Cryst.* 547:203–12
66. Yuan Y, Smalyukh II. 2015. *Opt. Lett.* 40:5630–33
67. Liu Q, Campbell M, Evans JS, Smalyukh II. 2014. *Adv. Mater.* 26:7178–84
68. Burylov SV, Raikher YL. 1994. *Phys. Rev. E* 50:358–67
69. Liu Q, Tang J, Zhang Y, Martinez A, Wang S, et al. 2014. *Phys. Rev. E* 89:052505
70. Trivedi RP, Lee T, Bertness T, Smalyukh II. 2010. *Opt. Express* 18:27658–69
71. Burylov SV, Zakhlevnykh AN. 2013. *Phys. Rev. E* 88:012511
72. Lapointe CP, Hopkins S, Mason TG, Smalyukh II. 2010. *Phys. Rev. Lett.* 105:178301
73. Gardner DF, Evans JS, Smalyukh II. 2011. *Mol. Cryst. Liq. Cryst.* 545:1227–45
74. Conradi M, Zorko M, Muševič I. 2010. *Opt. Express* 18:500–6
75. Tkalec U, Muševič I. 2013. *Soft Matter* 9:8140–50
76. Lapointe CP, Mason TG, Smalyukh II. 2011. *Opt. Express* 19:18182–89
77. Engström D, Trivedi RP, Persson M, Goksör M, Bertness KA, Smalyukh II. 2011. *Soft Matter* 7:6304–12
78. Tamura Y, Kimura Y. 2016. *Appl. Phys. Lett.* 108:011903
79. Senyuk B, Evans JS, Ackerman PJ, Lee T, Manna P, et al. 2012. *Nano Lett.* 12:955–63
80. Liu Q, Yuan Y, Smalyukh II. 2014. *Nano Lett.* 14:4071–77
81. Matthias H, Kitzerow H-S. 2009. *Mol. Cryst. Liq. Cryst.* 508:127–36
82. Senyuk B, Glugla D, Smalyukh II. 2013. *Phys. Rev. E* 88:062507
83. Twombly CW, Evans JS, Smalyukh II. 2013. *Opt. Express* 21:1324–34
84. Hashemi SM, Jagodič U, Mozaffari MR, Ejtehadi MR, Muševič I, Ravnik M. 2017. *Nat. Commun.* 8:14026
85. Senyuk B, Smalyukh II. 2012. *Soft Matter* 8:8729–34
86. Stratford K, Henrich O, Lintuvuori JS, Cates ME, Marenduzzo D. 2014. *Nat. Commun.* 5:3954
87. Engström D, Varney MCM, Persson M, Trivedi RP, Bertness KA, et al. 2012. *Opt. Express* 20:7741–48
88. Trivedi RP, Engström D, Smalyukh II. 2011. *J. Opt.* 13:044001
89. Freiser MJ. 1970. *Phys. Rev. Lett.* 24:1041–43
90. Milnor JW. 1965. *Topology from the Differentiable Viewpoint*. Charlottesville: Univ. Va. Press

91. Senyuk B, Liu Q, He S, Kamien RD, Kusner RB, et al. 2013. *Nature* 493:200–5
92. Liu Q, Senyuk B, Tasinkevych M, Smalyukh II. 2013. *PNAS* 110:9231–36
93. Martinez A, Ravnik M, Lucero B, Visvanathan R, Žumer S, Smalyukh II. 2014. *Nat. Mater.* 13:258–63
94. Martinez A, Hermosillo L, Tasinkevych M, Smalyukh II. 2015. *PNAS* 112:4546–51
95. Senyuk B, Behabtu N, Martinez A, Lee T, Tsentalovich DE, et al. 2015. *Nat. Commun.* 6:7157
96. Park S, Liu Q, Smalyukh II. 2016. *Phys. Rev. Lett.* 117:277801
97. Machon T, Alexander GP. 2013. *PNAS* 110:14174–79
98. Hung FR, Guzmán O, Gettelfinger BT, Abbott NL, de Pablo JJ. 2006. *Phys. Rev. E* 74:011711
99. Hung FR. 2009. *Phys. Rev. E* 79:021705
100. Senyuk B, Liu Q, Yuan Y, Smalyukh II. 2016. *Phys. Rev. E* 93:062704
101. Gharbi MA, Cavallaro MJ, Wu G, Beller DA, Kamien RD, et al. 2013. *Liq. Cryst.* 40:1619–27
102. Senyuk B, Pandey MB, Liu Q, Tasinkevych M, Smalyukh II. 2015. *Soft Matter* 11:8758–67
103. Beller DA, Gharbi MA, Liu IB. 2015. *Soft Matter* 11:1078–86
104. Ravnik M, Čopar S, Žumer S. 2015. *J. Phys. Condens. Matter* 27:354111
105. Evans JS, Sun Y, Senyuk B, Keller P, Pergamenshchik VM, et al. 2013. *Phys. Rev. Lett.* 110:187802
106. Tasinkevych M, Mondiot F, Mondain-Monval O, Loudet JC. 2014. *Soft Matter* 10:2047–58
107. Rasna MV, Zuhail KP, Ramudu UV, Chandrasekar R, Dontabhaktuni J, Dhara S. 2015. *Soft Matter* 11:7674–79
108. Varney MCM, Zhang Q, Smalyukh II. 2015. *Phys. Rev. E* 91:052503
109. Antipova A, Denniston C. 2016. *Soft Matter* 12:1279–94
110. Senyuk B, Varney MCM, Lopez J, Wang S, Wu N, Smalyukh II. 2014. *Soft Matter* 10:6014–23
111. Dontabhaktuni J, Ravnik M, Žumer S. 2014. *PNAS* 111:2464–69
112. Silvestre N, Liu Q, Senyuk B, Smalyukh II, Tasinkevych M. 2014. *Phys. Rev. Lett.* 112:225501
113. Peng C, Turiv T, Zhang R, Guo Y, Shiyanovskii SV, et al. 2017. *J. Phys. Condens. Matter* 29:014005
114. Trivedi RP, Tasinkevych M, Smalyukh II. 2016. *Phys. Rev. E* 94:062703
115. Copar S, Porenta T, Ackerman PJ, Pandey MB, Varney MCM, et al. 2014. *Sci. Rep.* 4:7337
116. Pandey MB, Porenta T, Brewer J, Burkart A, Čopar S, et al. 2014. *Phys. Rev. E* 89:060502(R)
117. Zerrouki D, Baudry J, Pine D, Chaikin P, Bibette J. 2008. *Nature* 455:380–82
118. Uzunova VA, Pergamenshchik VM. 2011. *Phys. Rev. E* 84:031702
119. Jampani VSR, Škarabot M, Čopar S, Žumer S, Muševič I. 2013. *Phys. Rev. Lett.* 110:177801
120. Gvozdovskyy I, Jampani VSR, Škarabot M, Muševič I. 2013. *Eur. Phys. J. E* 36:97
121. Varney MCM, Jenness N, Smalyukh II. 2014. *Phys. Rev. E* 89:022505
122. Jampani VSR, Škarabot M, Ravnik M, Čopar S, Žumer S, Muševič I. 2011. *Phys. Rev. E* 84:031703
123. Lintuvuori JS, Stratford K, Cates ME, Marenduzzo D. 2010. *Phys. Rev. Lett.* 105:178302
124. Varney MCM, Zhang Q, Tasinkevych M, Silvestre N, Bertness KA, Smalyukh II. 2014. *Phys. Rev. E* 89:052505
125. Nych A, Ognysta U, Muševič I, Seč D, Ravnik M, et al. 2014. *Phys. Rev. E* 89:062502
126. Ackerman PJ, Smalyukh II. 2017. *Nat. Mater.* 16:426–32
127. Boles MA, Engel M, Talapin DV. 2016. *Chem. Rev.* 116:11220–89
128. Ackerman PJ, Mundoor H, Smalyukh II, van de Lagemaat J. 2015. *ACS Nano* 9:12392–400
129. Mundoor H, Lee H, Gann DG, Ackerman PJ, Senyuk B, et al. 2014. *J. Appl. Phys.* 116:063511
130. Rovner JB, Reich DH, Leheny RL. 2013. *Langmuir* 29:2104–7
131. Noël CM, Bossis G, Chaze A-M, Giulieri F, Lacis S. 2006. *Phys. Rev. Lett.* 96:217801
132. Gharbi MA, Nobili M, In M, Prévot G, Galatola P, et al. 2011. *Soft Matter* 7:1467–71
133. Kim S-J, Kim J-H. 2014. *Soft Matter* 10:2664–70
134. Lev BI, Fukuda J, Tovkach OM, Chernyshuk SB. 2014. *Phys. Rev. E* 89:012509
135. Tovkach OM, Chernyshuk SB, Lev BI. 2015. *Phys. Rev. E* 92:042505
136. Mozaffari MR, Babadi M, Fukuda J, Ejtehadi MR. 2011. *Soft Matter* 7:1107–13
137. Chernyshuk SB. 2014. *Eur. Phys. J. E* 37:6
138. Lee B-K, Kim S-J, Lev B, Kim J-H. 2017. *Phys. Rev. E* 95:012709
139. Trushkevych O, Ackerman P, Crossland WA, Smalyukh II. 2010. *Appl. Phys. Lett.* 97:201906
140. Nayek P, Karan S, Kundu S, Lee SH, Gupta SD, et al. 2012. *J. Phys. D Appl. Phys.* 45:235303
141. Sun Y, Evans JS, Lee T, Senyuk BI, Keller P, et al. 2012. *Appl. Phys. Lett.* 100:241901

142. Kalakonda P, Basu R, Nemitz IR, Rosenblatt C, Iannacchione GS. 2014. *J. Chem. Phys.* 140:104908
143. Evans JS, Ackerman PJ, Broer DJ, van de Lagemaat J, Smalyukh II. 2013. *Phys. Rev. E* 87:032503
144. Lukach A, Thérein-Aubin H, Querejeta-Fernández A, Pitch N, Chauve G, et al. 2015. *Langmuir* 31:5033–41
145. Smalyukh II, Butler J, Shrout JD, Parsek MR, Wong GCL. 2008. *Phys. Rev. E* 78:030701(R)
146. Lavrentovich OD. 2016. *Curr. Opin. Colloid Interface Sci.* 21:97–109
147. Mushenheim PC, Trivedi RR, Tuson HH, Weibel DB, Abbott NL. 2014. *Soft Matter* 10:79–86
148. Trivedi RR, Maeda R, Abbott NL, Spagnolie SE, Weibel DB. 2015. *Soft Matter* 11:8404–8
149. Genkin MM, Sokolov A, Lavrentovich OD, Aranson IS. 2017. *Phys. Rev. X* 7:011029
150. Marchetti MC, Joanny JF, Ramaswamy S, Liverpool TB, Prost J, et al. 2013. *Rev. Mod. Phys.* 85:1143–89

Annual Review
of Condensed
Matter Physics

Volume 9, 2018

Contents

Errata

An online log of corrections to *Annual Review of Condensed Matter Physics* articles may be found at http://www.annualreviews.org/errata/conmatphys